JACS
JOURNAL OF THE AMERICAN CHEMICAL SOCIETY
Article
Cite This: J. Am. Chem. Soc. 2017, 139, 15940-15949
pubs.acs.org/JACS

Antitumor Activity of a Unique Polymer That Incorporates a Fluorescent Self-Assembled Metallacycle

Guocan Yu,[†] Mingming Zhang,[‡] Manik Lal Saha,[‡] Zhengwei Mao,[*,§] Jin Chen,[§] Yong Yao,[‡] Zijian Zhou,[†] Yijing Liu,[†] Changyou Gao,[§] Feihe Huang,[*,∥] Xiaoyuan Chen,[*,†] and Peter J. Stang[*,‡]

[†]Laboratory of Molecular Imaging and Nanomedicine, National Institute of Biomedical Imaging and Bioengineering, National Institutes of Health, Bethesda, Maryland 20892, United States

[‡]Department of Chemistry, University of Utah, 315 South 1400 East, Room 2020, Salt Lake City, Utah 84112, United States

[§]MOE Key Laboratory of Macromolecular Synthesis and Functionalization, Department of Polymer Science and Engineering, Zhejiang University, Hangzhou 310027, P. R. China

[∥]State Key Laboratory of Chemical Engineering, Center for Chemistry of High-Performance & Novel Materials, Department of Chemistry, Zhejiang University, Hangzhou 310027, P. R. China

Supporting Information

ABSTRACT: Despite the well-known anticancer activity of mono- and multinuclear platinum complexes, studies of the antitumor performances of platinum-based supramolecular coordination complexes are rare. Herein, we report on the synthesis of a four-armed amphiphilic copolymer, **Pt-PAZMB-*b*-POEGMA**, containing a metallacycle **M**, in which the tetraphenylethene derivative acts as an aggregation-induced emissive fluorescent probe for live cell imaging and the 3,6-bis[*trans*-Pt(PEt_3)$_2$]phenanthrene (**PhenPt**) is an anticancer drug. This copolymer was further self-assembled into nanoparticles of different sizes and vesicles depending upon the experimental conditions. The impacts of the morphology and size of the assemblies on their endocytic pathways, uptake rates, internalization amounts, and cytotoxicities were investigated. The self-assemblies were further employed to encapsulate doxorubicin (DOX) to achieve a synergistic anticancer effect. Controlled drug release was also realized via amphiphilicity changes and was driven by a glutathione-induced cascade elimination reaction. The DOX-loaded nanoparticles of around 50 nm in size exhibited an excellent antitumor performance as well as a low systemic toxicity, due to an enhanced permeability and retention effect.

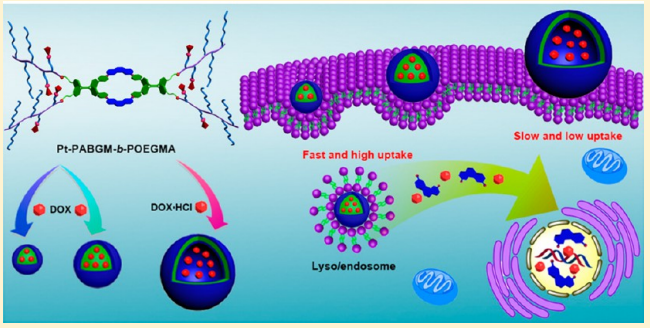

INTRODUCTION

Over the past few decades, discrete supramolecular coordination complexes (SCCs) with well-defined size, shape, and geometry have received increasing attention not only for their aesthetic attributes but also because of their wide applications in sensors, catalysis, amphiphilic self-assembly, host−guest chemistry, supramolecular polymers, and biomedicines.[1] Many sophisticated 2D metallacycles and 3D metallacages have been developed through the judicious choice of metals and ligands.[2] Due to the anticancer activity of organometallic ruthenium and platinum complexes, therapeutic SCCs, including these metals as the acceptors, have been prepared in recent years.[3] Different from the clinical drugs, such as cisplatin, imaging capability can also be integrated into these SCC platforms by simply choosing fluorescent ligands as the coordination donors. This subsequently helps to trace the delivery and release of the organometallic drug *in vitro* and *in vivo*.[4] Nevertheless, for biomedical applications the stability of the SCCs in a physiological environment needs to be improved, because the metals (e.g., Fe, Cu, and Zn) and amino acids in blood can potentially dissociate the SCCs, thereby causing side effects as well as erroneous imaging results. The limited solubility and often poor tumor accumulation of the SCCs are the other major obstacles. Physical encapsulation by copolymers and chemical modification of SCCs have emerged as the two effective ways to solve these problems. In particular, the postmodification of SCCs with amphiphilic copolymers is a good method to fabricate drug delivery systems (DDSs), because this can enhance the solubility and the stability of a given SCC in aqueous medium as well as allows to load other anticancer drug(s) into the polymeric scaffold, with a possibility of having a synergistic anticancer effect. Moreover, stimuli-responsiveness can be incorporated into these systems to amplify the therapeutic efficiency and to reduce the possible side effects.[5]

Fluorescence imaging techniques have been widely used in the investigation of biological processes, that subsequently led

Received: August 29, 2017
Published: October 11, 2017

DOI: 10.1021/jacs.7b09224
J. Am. Chem. Soc. 2017, 139, 15940−15949

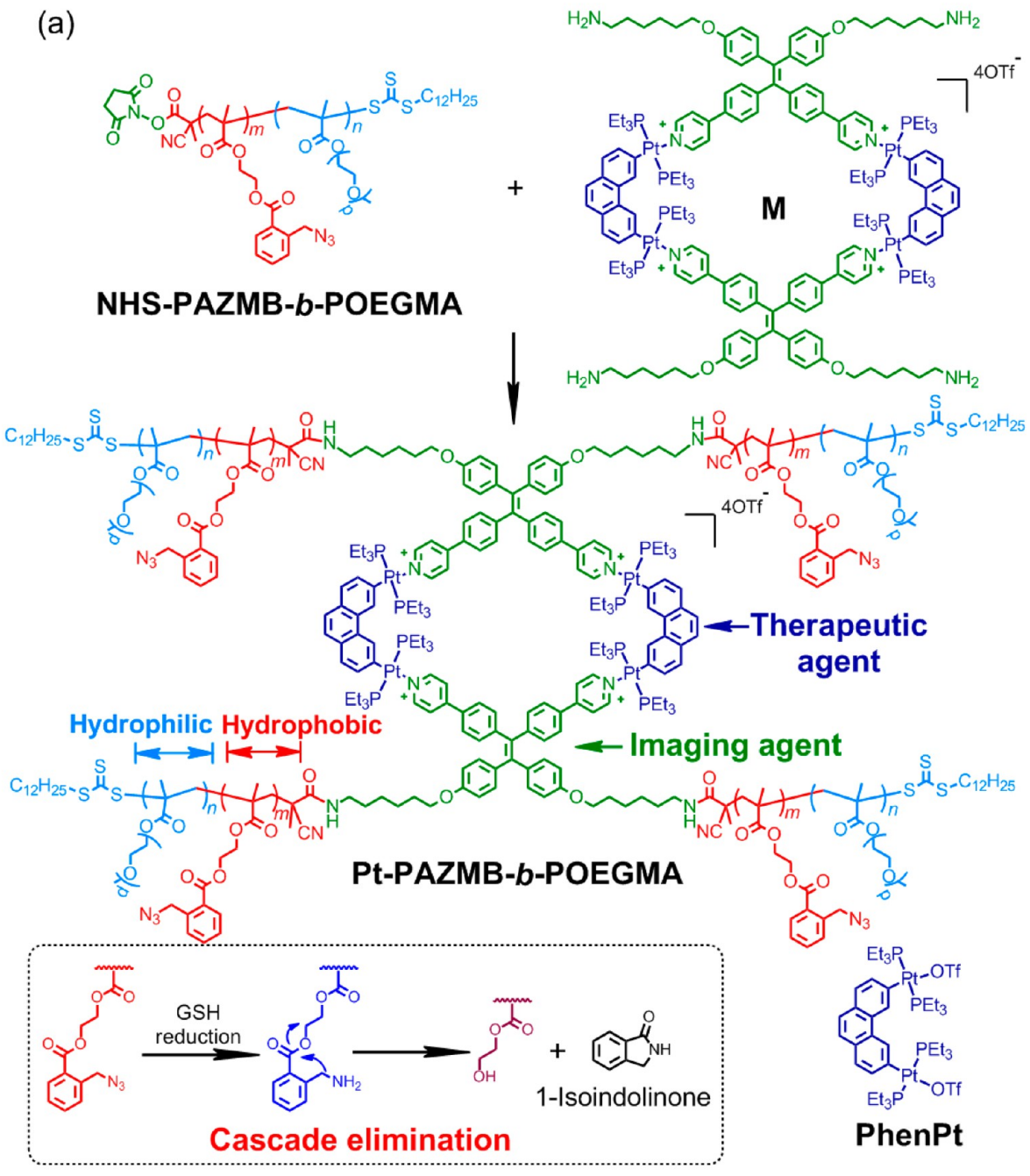

Figure 1. continued

DOI: 10.1021/jacs.7b09224
J. Am. Chem. Soc. 2017, 139, 15940−15949

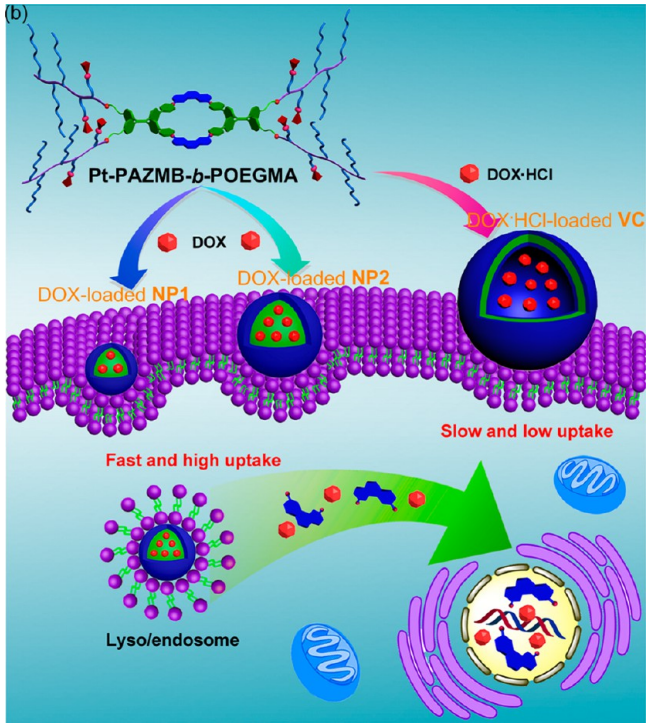

Figure 1. (a) Synthesis of **Pt-PAZMB-*b*-POEGMA** and its GSH-triggered amphiphilicity reversion mechanism. (b) Cartoon illustration of the cellular uptake of DOX-loaded nanostructures self-assembled from **Pt-PAZMB-*b*-POEGMA**.

to the development of novel imaging-guided therapeutic procedures.[6] However, conventional fluorophores often suffer from an undesirable aggregation-caused quenching (ACQ) effect, greatly limiting their biomedical applications.[7] In contrast, Tang et al. demonstrated aggregation-induced emission (AIE), wherein AIE-active fluorophores (AIEgens) are nearly nonemissive as discrete molecules, but emit bright fluorescence in the aggregate state via the restriction of intramolecular motion mechanisms.[8] Recently, we employed supramolecular coordination to restrict the intramolecular rotation of AIEgens,[9] making them with high fluorescent in both solutions and aggregated state. These features endow AIEgens-based SCCs with better photostability, making them promising candidates for cell imaging.

Herein, we develop an amphiphilic polymer **Pt-PAZMB-*b*-POEGMA**, containing glutathione (GSH)-responsive diblock copolymers as the arms and an aggregation-induced emissive metallacycle **M** as the core (Figure 1). This polymer further self-assembled into nanoparticles (**NPs**) of different sizes (**NP1** and **NP2**) and vesicles (**VC**) via a re-precipitation, dialysis, and double-emulsion technique, respectively. Due to their different morphology and size, these assemblies follow distinct endocytic pathways and have different internalization rates and cytotoxicities toward HeLa cells. Notably, the **NPs** and **VC** are capable of encapsulating neutral doxorubicin (DOX) and doxorubicin hydrochloride (DOX·HCl), respectively. The amphiphilicity of the polymer **Pt-PAZMB-*b*-POEGMA** was altered via a GSH-triggered cascade elimination of the hydrophobic protection groups, resulting in the disassembly of the nanostructures and the subsequent release of the loaded chemotherapeutic agent. The *in vitro* and *in vivo* studies demonstrated that the **NPs** with a diameter of 50 nm are the best candidates to co-deliver **PhenPt** and DOX in a synergistic manner that can effectively suppress tumor growth with a negligible systemic toxicity.

RESULTS AND DISCUSSION

Synthesis and Self-Assembly of Pt-PAZMB-*b*-POEGMA. As shown in Figure 1a, **Pt-PAZMB-*b*-POEGMA** was synthesized via an amidation reaction between **NHS-PAZMB-*b*-POEGMA** and metallacycle **M**[10c] (Scheme S1 and Figures S1−S7), where the polymer precursor **NHS-PAZMB-*b*-POEGMA** was obtained via a reversible addition−fragmentation chain-transfer polymerization reaction. The material was fully characterized by multinuclear NMR (^{31}P and ^{1}H) and gel permeation chromatography (GPC) analyses. The sharp singlet at 9.07 ppm with concomitant ^{195}Pt satellites in the ^{31}P{^{1}H}-NMR spectrum of **Pt-PAZMB-*b*-POEGMA** supports the presence of **M** in this material (Figure S8). Likewise, the ^{1}H NMR resonances in the range of 6.50−9.00 ppm are diagnostic for the metallacyclic core of the polymer (Figure S5). Moreover, the number-averaged molecular weight increased to 89.7 kDa in the GPC curves upon the formation of **Pt-PAZMB-*b*-POEGMA** (Figure 2a), which is about 4-fold higher than that of the precursor **NHS-PAZMB-*b*-POEGMA** (20.1 kDa), thereby supporting the formation of a four-armed copolymer.

For both **M** and **Pt-PAZMB-*b*-POEGMA**, the emissions of the TPE-based dipyridyl donors are significantly enhanced (Figures 2b and S12) relative to that of the free ligand. This is because in these materials the Pt ← pyridyl coordination interactions somewhat restricted the intramolecular rotations of the TPE units and thus impart a better emission.[6] The polymer also exhibits an AIE property. As shown in Figure 2b, the emission intensity of an acetone solution of the polymer gradually increased upon the incremental addition of water. In contrast, the emission of an acetone solution containing only **M** decreased when the water fraction (f_w) increased from 0 to 40%, then increased with a further increase of f_w (Figures 2b and S11). The reason is that the solubility of **M** is poor in both

DOI: 10.1021/jacs.7b09224
J. Am. Chem. Soc. 2017, 139, 15940−15949

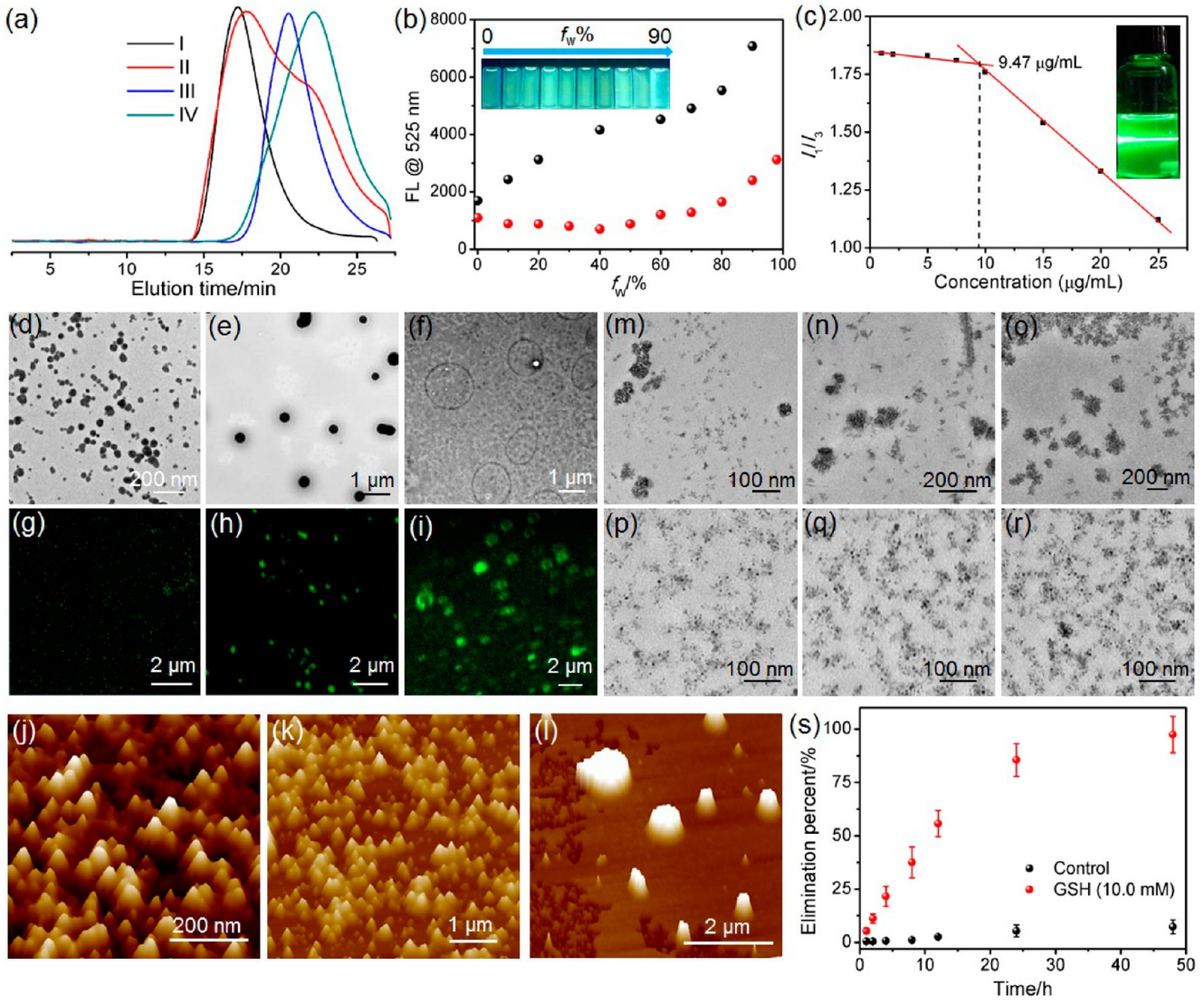

Figure 2. (a) GPC curves of (I) **Pt-PAZMB-*b*-POEGMA**, (II) **Pt-PAZMB-*b*-POEGMA** before purification, (III) **Pt-PAZMB-*b*-POEGMA** after GSH treatment, and (IV) **NHS-PAZMB-*b*-POEGMA**. (b) Fluorescence intensity of **Pt-PAZMB-*b*-POEGMA** (black dots) and **M** (red dots) at 525 nm vs. f_w of the aqueous mixtures. Inset: a fluorescent photo of **Pt-PAZMB-*b*-POEGMA** in mixtures of THF and water with different f_w values. (c) CAC value determination of **Pt-PAZMB-*b*-POEGMA** by using pyrene as a probe. Inset: Tyndall effect of the aqueous solution when the concentration of **Pt-PAZMB-*b*-POEGMA** was higher than its CAC value. TEM (d–f), CLSM (g–i), and AFM (j–l) images of **NP1** (d,g,j), **NP2** (e,h,k), and **VC** (f,i,l). TEM images of **NP1** (m,p), **NP2** (n,q), and **VC** (o,r) after GSH treatment for 4 h (m–o) and 24 h (p–r). (s) Elimination of **AZMB** in the absence and presence of GSH (10.0 mM).

pure acetone and water, while it can be better dissolved in their mixture. It should also be noted that **Pt-PAZMB-*b*-POEGMA** exhibited a much stronger AIE effect (Figure 2b) than free **M**, which is likely due to its polymeric structure. Likewise, the quantum yield (Φ_F) of **Pt-PAZMB-*b*-POEGMA** in methanol/water (1/9, *v*/*v*) was determined to be 3.16% by using quinine sulfate as the standard, which is higher than that of **M** (Φ_F = 1.22%).

By using fluorescence as a probe, the critical aggregation concentration (CAC) of the amphiphilic polymer **Pt-PAZMB-*b*-POEGMA** was determined to be 9.47 μg/mL (Figure 2c), which is much lower than that of the precursor **NHS-PAZMB-*b*-POEGMA** (CAC = 33.6 μg/mL) (Figure S13). Nanoparticles with diameters of around 50 (for **NP1**) and 500 nm (for **NP2**) were obtained from **Pt-PAZMB-*b*-POEGMA** by employing a reprecipitation and a dialysis method, respectively, and were characterized by transmission electron (TEM) (Figure 2d,e) and atomic force (AFM) microscopies (Figure 2j,k). Dynamic light scattering (DLS) studies revealed that the average diameter of **NP1** and **NP2** are 49.8 ± 5.2 and 429 ± 51.8 nm, respectively (Figures S16 and S17). In contrast, vesicles of 0.8–3.0 μm in diameter were obtained when **Pt-PAZMB-*b*-POEGMA** was subjected to a double emulsion technique. This material was also characterized by TEM (Figure 2f), AFM (Figure 2l) and DLS (Figure S18). The membrane thickness and height of **VC** are 7.2 ± 0.8 and 13 nm, respectively, as obtained from the TEM and AFM measurements. In the vesicles, the **POEGMA** segments construct the hydrophilic outer and inner layers, while the **PAZMB** portions form the hydrophobic core layer. Due to the AIE effect of the TPE units, the solutions of **NP1**, **NP2**, or **VC** are highly emissive (Figure S15) and were further characterized by confocal laser scanning microscopy (CLSM) (Figure 2g,h). The colloidal stability of these nanostructures was evidenced by the

DOI: 10.1021/jacs.7b09224
J. Am. Chem. Soc. 2017, 139, 15940–15949

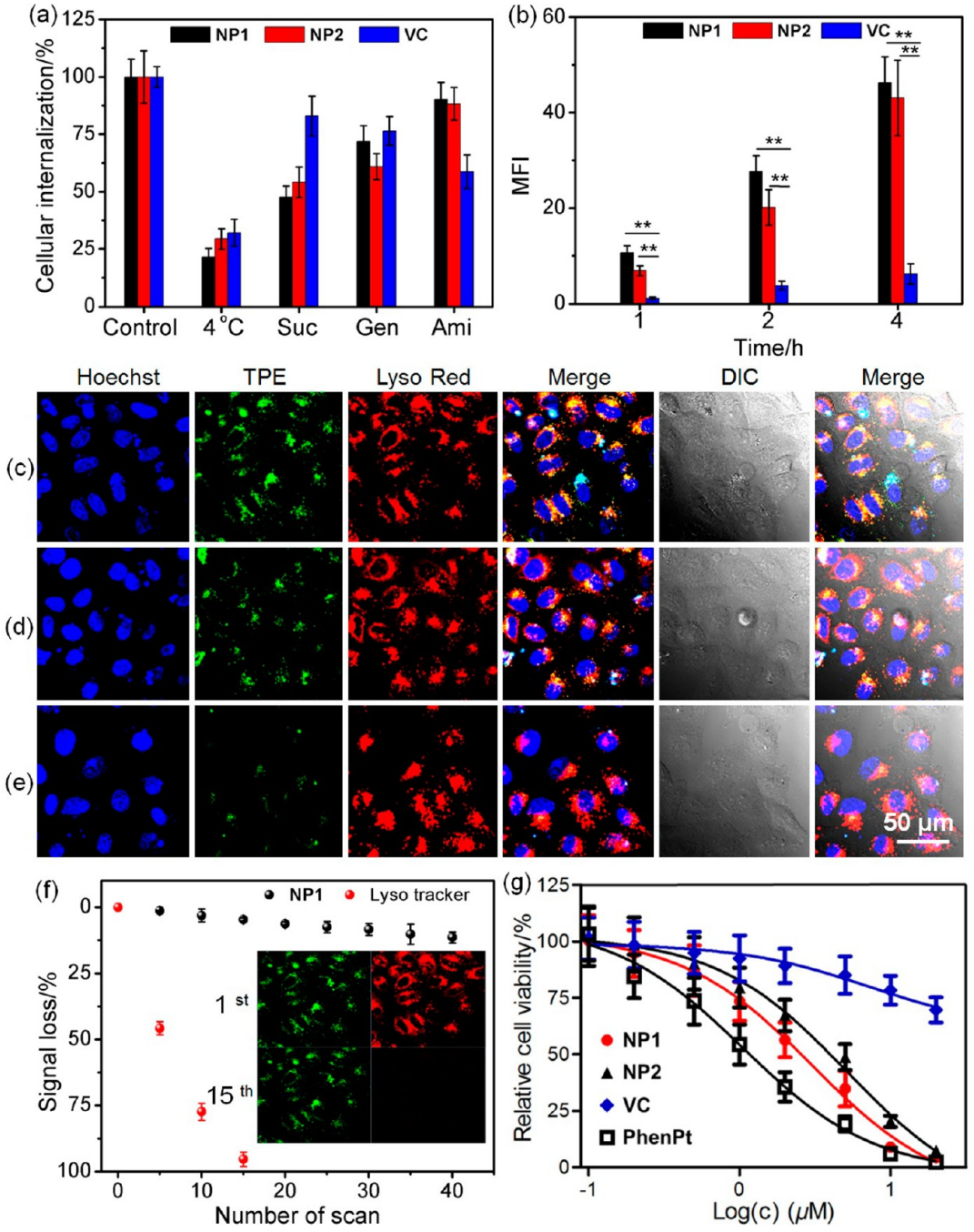

Figure 3. (a) Cellular internalization of **NP1**, **NP2**, and **VC** by HeLa cells in the absence and presence of various inhibitors. (b) Mean fluorescent intensity of the HeLa cells after treatment with **NP1**, **NP2**, and **VC** for different time periods (**$p < 0.01$). CLSM images of the HeLa cells incubated with (c) **NP1**, (d) **NP2**, and (e) **VC** for 8 h. (f) Signal loss of fluorescent emission of **NP1** and Lyso tracker Red with increasing number of scans. Inset: CLSM images of living HeLa cells after different number of scans. (g) Cytotoxicity of **NP1**, **NP2**, **VC**, and **PhenPt** toward HeLa cells after 24 h incubation.

fact that neither morphology nor size change was observed over a period of 2 months.

Size-Dependent Endocytosis and Anticancer Effect of the Nanostructures. Nanostructures depending upon their morphology and size can enter into cells via several different endocytic pathways. This not only affects the uptake efficiency but also influences their intracellular fate and subsequently results in different pharmacological activities of the loaded cargos (such as dyes, drugs, or genes).[11] The internalization pathways of **NP1**, **NP2**, and **VC** into HeLa cells were investigated using a flow cytometry (FCM) technique, in the presence of various endocytosis inhibitors. The results suggest that the cellular uptake for all assemblies is greatly inhibited at 4 °C (Figure 3a), indicating that these pathways are energy-dependent.[11a] The uptakes of **NP1** and **NP2** into HeLa cells were also effectively suppressed in the presence of sucrose (Suc), while negligible effects were observed for genistein (Gen) and amiloride-HCl (Ami). These data collectively indicate that the **NPs** are mainly internalized via a clathrin-mediated endocytic pathway,[11b] allowing the **NPs** to undergo

DOI: 10.1021/jacs.7b09224
J. Am. Chem. Soc. 2017, 139, 15940−15949

an intracellular endo/lysosomal transportation. This was further supported by the CLSM images that exhibit a good overlap between the green fluorescence of the TPE units and the red fluorescence of the Lyso tracker Red dye (Figure 3c,d). In contrast, a 41.3% decrease in the cellular uptake was observed for **VC** in the presence of Ami, suggesting that a macropinocytosis mediated pathway drives the internalization of **VC**.

The time-dependent internalization of **NP1**, **NP2**, and **VC** was further studied by FCM, CLSM, and inductively coupled plasma mass spectrometry (ICP-MS). Compared to the large-sized **VC**, a faster uptake rate and a higher intracellular accumulation were observed for both **NPs**, as evidenced from the FCM (Figure 3b) and ICP-MS data. Likewise, the amount of platinum in the cells treated with **NP1**, **NP2**, and **VC** for 4 h was 79.3 ± 8.2, 70.7 ± 6.7, and 6.4 ± 0.8 ng/10^6 cells (Figure S19), respectively, revealing that the uptakes of **NP1** and **NP2** by HeLa cells are more efficient than that of **VC**. In the CLSM images, we also observed that the green fluorescence intensity of the cells treated with either **NP1** or **NP2** was higher compared to those examined in the presence of **VC** (Figure 3c–e). This also supports the above results.

The nanoassemblies displayed a better photostability compared to the conventional fluorophores. As shown in Figure 3f, a 11.4% loss of fluorescence signal was observed for **NP1** after 40 scans, while the red fluorescence of Lyso tracker Red completely disappeared after only 15 scans. This suggests that the latter fluorescence was photobleached by the excitation light at this low working concentration, while for **NP1**, the AIE-active metallacycles were not photobleached or photo-oxidized under a similar condition, thus maintaining its emission.

The anticancer mechanism of platinum-based drugs relies on their ability to coordinate with the purine bases of DNA, interfering with the DNA repair mechanisms, causing DNA damage, and subsequently inducing cell apoptosis.[12] To mimic the coordination interactions between **PhenPt** and DNA, several control experiments were performed. Guanosine triphosphate (GTP) was utilized as a competitive ligand to study the disassembly of the metallacycle **M** via fluorescence spectroscopy.[4a] A significant fluorescence quenching was observed after incubating an aqueous solution of **M** with GTP (Figure S20), suggesting that GTP is a suitable donor for **PhenPt** and can disassemble the metallacycle. Next, the metallacycle **M** was gradually added to a solution containing calf-thymus DNA (ctDNA), and the relative viscosity (η/η_0) of the resulting solution was increased, indicating the formation of ctDNA/Pt coordination complex (Figure S21). The interactions between **M** and DNA were also examined by a fluorescence displacement experiment using ethidium bromide (EB) as a control. The fluorescence intensity of the ctDNA/EB complex was decreased upon a gradual addition of **M**, pointing toward the competitive binding of **M** to ctDNA (Figure S22). These studies demonstrate that the metallacycles in the nanostructures are able to cross-link with DNA.

The anticancer efficacies of **NP1**, **NP2**, and **VC** were evaluated using a 3-(4′,5′-dimethylthiazol-2′-yl)-2,5-diphenyl tetrazolium bromide (MTT) assay. For the precursor **NHS-PAZMB-*b*-POEGMA**, negligible changes in the relative cell viability were observed even when its concentration reached 1.00 mg/mL (Figure S23). The half-maximal inhibitory concentrations (IC_{50}) are 2.89 ± 0.31 and 5.84 ± 0.63 μM for **NP1** and **NP2** (Figure 3g), respectively. These values are much lower than that of **VC** (IC_{50} > 20 μM) but are comparable with that of **PhenPt** (IC_{50} = 1.06 ± 0.15 μM), demonstrating that the anticancer efficacy of the organometallic drug was maintained in the nanoparticles, due to their rapid and efficient internalizations in the cells.

GSH-Responsive Disassembly and Controlled Drug Release. Notably, the 2-azido-methylbenzoate (**AZMB**) units of the polymer **Pt-PAZMB-*b*-POEGMA** are self-cleavable groups and can be easily removed via a cascade elimination reaction triggered by the intracellular reducing agents, such as GSH (Figure 1).[13] As a consequence, the amphiphilicity of the polymer backbone was altered, resulting in a disassembly of the nanostructures. The GSH-responsive detachment of the **AZMB** units was first studied in a dialysis medium by monitoring the absorption band centered at ca. 250 nm that corresponds to the absorption of the released byproduct, 1-isoindolinone. In the absence of stimulus, the absorption of the dialysis solution remained constant (Figure 2s), while the elimination percentage of **AZMB** gradually increased in the presence of 10.0 mM GSH over a period of 48 h. Likewise, in the ^{1}H NMR spectrum of **NHS-PAZMB-*b*-POEGMA**, the peaks for the protons on the **AZMB** units, ranging from 7.25 to 8.10 ppm, entirely disappeared after 48 h (Figure S24), suggesting that a complete elimination was accomplished. Further characterization of this process was performed via GPC studies, where a decrease in molecular weight from 89.7 to 58.3 kDa was observed after the copolymer solution was exposed to GSH for 24 h (Figure 2a). TEM images indicated that **NP1**, **NP2**, and **VC** split into irregular aggregates after being exposed to GSH for 4 h, likely indicating a partial cleavage of the **AZMB** units (Figure 2m–o). However, a prolonged incubation of 24 h resulted in a complete disassembly of the nanostructures (Figure 2p–r). These processes were also monitored via DLS studies (Figures S28–S30), and the results are in agreement with the TEM images.

These GSH-responsive nanostructures were further employed as DDSs to encapsulate antitumor drugs and to achieve a synergistic anticancer effect. The hydrophobic cores of **NP1** and **NP2** are suitable platforms to load neutral DOX, whereas the hollow cavity of **VC** can encapsulate DOX·HCl. Only slight changes were observed in their sizes after loading the drugs (Table 1), while no obvious size variation was detected in a PBS containing 10% fetal bovine serum over 48 h at 37 °C. This indicates that these drug-loaded nanostructures are stable in this medium (Figures S33–S35). GSH-responsive drug release was observed due to the disassembly of the nanocarriers (Figures S36–S38). The pH-responsive drug release was also

Table 1. Drug Encapsulation and Size Determination of the DOX-Loaded Nanostructures

	polymer	drug loading content (%)[a]	Pt content (%)[b]	average diameter (nm)[c]
NP1	**Pt-PAZMB-*b*-POEGMA**	27.4	0.631	57.2
NP2	**Pt-PAZMB-*b*-POEGMA**	33.6	0.577	487.1
VC	**Pt-PAZMB-*b*-POEGMA**	14.2	0.746	1483.6
NP3	**NHS-PAZMB-*b*-POEGMA**	23.1	0	48.3

[a]Drug loading content was determined by using UV–vis spectroscopy. [b]Pt content in the nanostructures was calculated based on the mass of polymers and loaded drug. [c]The average diameter of the drug-loaded nanostructures was determined by using DLS.

DOI: 10.1021/jacs.7b09224
J. Am. Chem. Soc. 2017, 139, 15940–15949

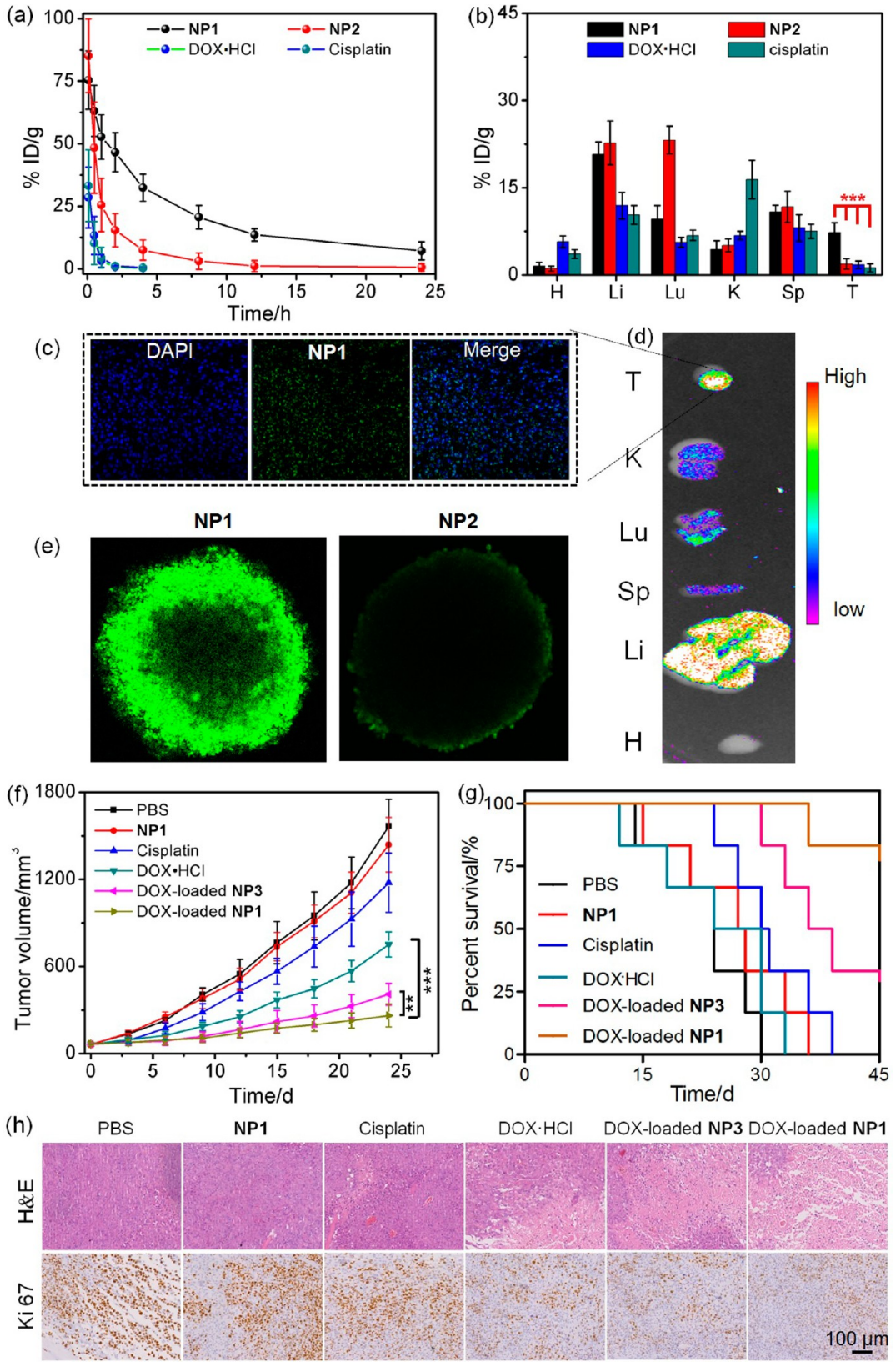

Figure 4. (a) Blood circulation time of **NP1**, **NP2**, DOX·HCl, and cisplatin in normal mice after i.v. injection. (b) Tissue distributions of **NP1**, **NP2**, DOX·HCl, and cisplatin in the main organs at 24 h post-injection. Data are expressed as means ± s.d. (n = 3), ***P < 0.001. (c) CLSM images of the intratumor distribution of **NP1**. (d) Fluorescence images of isolated organs separated from HeLa tumor-bearing mice at 24 h post injection of **NP1**. (e) CLSM images showing *in vitro* penetration of **NP1** and **NP2** in HeLa multicellular spheroids. (f) Tumor growth inhibition curves and (g) survival rate of the mice bearing HeLa tumors after different treatments. Data are expressed as means ± s.d. (n = 6), **P < 0.01, ***P < 0.001. (h) H&E and Ki67 analyses of tumor tissues after various formulations. The dosage of DOX and Pt in these administrations was kept at 5.00 and 0.150 mg/kg, respectively.

DOI: 10.1021/jacs.7b09224
J. Am. Chem. Soc. 2017, 139, 15940−15949

realized for DOX-loaded **NP1** and DOX-loaded **NP2** due to the protonation of the amine group of DOX.

By taking advantage of the intrinsic fluorescence emission of DOX, CLSM was employed to confirm the accumulation of DOX-loaded nanostructures. After being internalized by endocytosis and transported into endo/lysosomes (Figure S43), the green fluorescence of **NP1** and the red fluorescence of DOX were both observed in the cytoplasm after a 4 h treatment. By extending the culture time to 24 h, the loaded DOX was successfully released due to the disassembly of the nanostructures. The released DOX accumulated into the nuclei, where the anticancer activity took place (Figure S44). Both **NHS-PAZMB-*b*-POEGMA** and the cleaved product indolin-1-one are nontoxic at all concentrations that were used in this study (Figure S23). Thus, any influence on cell viability from the DOX-loaded nanostructures is due to the toxicity of DOX and **PhenPt**. The IC_{50} values of free DOX, DOX-loaded **NP1**, DOX-loaded **NP2**, and DOX·HCl-loaded **VC** were determined to be 0.91 ± 0.10, 4.75 ± 0.52, 9.08 ± 0.89, and >25 μM, respectively (Figure S45). In order to calculate the combination index (CI) to confirm the presence of any synergistic effect, **NP3** of about 50 nm in diameter was prepared from the precursor **NHS-PAZMB-*b*-POEGMA**. The size and drug loading content of DOX-loaded **NP3** are comparable to those of DOX-loaded **NP1**, although the IC_{50} value of the former increased to 6.61 ± 0.74 μM, likely due to the absence of **PhenPt**. The CI value was calculated to be about 0.79 for DOX-loaded **NP1**, demonstrating a good synergistic anticancer effect present in the nanomedicine. Likewise, these nanostructures were also utilized as carriers for paclitaxel (PTX) (Table S1), demonstrating that **Pt-PAZMB-*b*-POEGMA** is a robust drug delivery platform for hydrophobic anticancer drugs. Controlled drug release (Figures S40−S42) and cytotoxicity (Figure S46) studies were also conducted to evaluate the GSH-responsive drug release and anticancer efficacy of the PTX-loaded nanostructures. An MTT assay confirmed that PTX-loaded **NP1** maintained the anticancer efficacy of PTX and possessed highest cytotoxicity toward the MDA-MB-231 cell line among the PTX-loaded nanostructures (PTX-loaded **NP1**, PTX-loaded **NP1**, and PTX-loaded **VC**) due to the rapid and efficient cellular internalization (Figure S46).

***In Vivo* Drug Delivery and Antitumor Treatment.** Nanomedicines with suitable diameters preferentially leak into tumor tissues via a permeable tumor vasculature and are then retained in the tumor due to the reduced lymphatic drainage.[14] Among these nanostructures, **NP1** appears to be the best candidate to deliver DOX *in vivo*, because its size falls within the optimal range. Moreover, the "brush like" PEG chains on the surface of **NP1** can prevent them from being adsorbed by proteins and cleared from the body by the reticuloendothelial system (RES). These give the **NPs** a better opportunity to extravasate from the tumor vessels.[15] The pharmacokinetics of cisplatin, DOX·HCl, **NP1**, and **NP2** were examined in mice by intravenous (i.v.) injection (Figure 4a). The circulation half-life of **NP1** was 3.16 ± 0.28 h, which is much higher than those of cisplatin, DOX·HCl, and **NP2** (0.27 ± 0.04, 0.34 ± 0.05, and 0.53 ± 0.47 h, respectively), thereby confirming that the blood circulation time of **NP1** is relatively long. Biodistribution studies also showed that only a small amount of cisplatin, DOX·HCl, and **NP2** appeared in the tumor region after 24 h post injection. In contrast, **NP1** resulted in remarkably higher tumor accumulation (Figure 4b). CLSM images (Figure 4c), *ex vivo* fluorescence images (Figure 4d), and multicellular spheroids staining (Figure 4e) also demonstrated that **NP1** exhibited a high tumor accumulation and an excellent tumor penetration capability due to its suitable size.

To evaluate the *in vivo* antitumor efficacy, HeLa tumor-bearing mice were intravenously injected with different formulations, including PBS, cisplatin, **NP1**, DOX·HCl, DOX-loaded **NP3**, and DOX-loaded **NP1**. The tumors treated with PBS grew exponentially over time and exhibited an average tumor volume of 1566 mm^3 after 21 days (Figure 4f). For the mice administered with cisplatin or blank **NP1** (0.150 mg Pt/kg), a very limited delay of the tumor growth was observed, due to the low drug dosage. In the DOX·HCl-treatment group, a moderate tumor inhibition was achieved, with the mean tumor volume of 752 mm^3 after 21 days. Due to the enhanced permeability and retention (EPR) effect and GSH-triggered drug release, DOX-loaded **NP3** exhibited a higher antitumor efficiency than free DOX·HCl. Notably, the DOX-loaded **NP1** formulation vastly outperforms all the other groups in reducing tumor volume. This is likely due to the aforesaid synergistic anticancer effect. After treatment, the tumors were also excised and weighed. Accordingly, the tumor inhibition rates were 5.74, 19.5, 45.9, 62.3, and 81.6% for cisplatin, **NP1**, DOX·HCl, DOX-loaded **NP3**, and DOX-loaded **NP1**, respectively (Figure S48), further suggesting a better antitumor activity of DOX-loaded **NP1**. The therapeutic efficacy of DOX-loaded **NP1** was also examined by a hematoxylin/eosin (H&E) staining and a nuclear non-histone protein (Ki67) staining. Among these therapeutic groups, the tumor tissues from the mice treated with DOX-loaded **NP1** exhibited the highest level of necrosis and the fewest proliferating cells, indicating a massive remission of proliferative activity (Figure 4h).

To assess the systemic toxicity of DOX-loaded **NP1**, we also compared the impact of different formulations on body weight, survival rate, organ histology and blood chemistry. Serious body weight fluctuations were observed for mice treated with free DOX·HCl, reflecting the huge side effects of DOX. In contrast, the group treated with DOX-loaded **NP1** did not show a significant body weight loss over the experimental period, indicating that a much reduced systemic toxicity can be achieved via the nanoformulation (Figure S49). In comparison with other groups (24, 27, 31, 28, and 38 days for PBS, cisplatin, **NP1**, DOX·HCl, and DOX-loaded **NP3**, respectively), the median survival of the mice treated with DOX-loaded **NP1** was significantly extended (Figure 4g), due to its excellent antitumor efficacy and low systemic toxicity. Histological analysis of major organ slices of the mice treated with free DOX showed severe cardiotoxicity, which was characterized by the notable vacuolization in the cardiomyocytes (Figure S50). For DOX-loaded **NP1**, the H&E staining images of the heart, liver, spleen, lung, and kidney revealed that all of the organs were normal. Moreover, blood biochemistry and hematology surveys were conducted after the administration of DOX-loaded **NP1** (Figure S51) on the 15th day with alanine aminotransferase, aspartate aminotransferase, alkaline phosphatase, red blood cells, white blood cells, creatinine, and blood urea nitrogen. Compared with the normal mice, all parameters were within normal range, further confirming that no liver or renal dysfunction were induced by the DOX-loaded **NP1**.

DOI: 10.1021/jacs.7b09224
J. Am. Chem. Soc. 2017, 139, 15940−15949

CONCLUSIONS

In summary, we developed a novel DDS platform consisting of a highly fluorescent metallacycle **M** and four GSH-responsive copolymeric arms. In the metallacycle, the emissive TPE-based bispyridyl ligands are the donors and act as a spectroscopic handle for live cell imaging, while the acceptor **PhenPt** units are employed as an anticancer drug. By using either a reprecipitation, dialysis or a double emulsion method, further self-assemblies of **NP1**, **NP2**, and **VC** were successfully prepared from this amphiphilic polymer. Due to differences in the morphology and size, these nanostructures exhibited different cytotoxicities toward HeLa cells. Furthermore, **NP1**, **NP2**, and **VC** can encapsulate DOX or DOX·HCl, while the release of the encapsulated drug was realized via a GSH-responsive elimination reaction. *In vitro* and *in vivo* investigations demonstrated that a co-delivery of DOX and **PhenPt** is possible with a synergistic anticancer effect. Given these results, this work provides valuable information and methodology for the rational design of the next generation DDSs based upon supramolecular structures.

ASSOCIATED CONTENT

Supporting Information

The Supporting Information is available free of charge on the ACS Publications website at DOI: 10.1021/jacs.7b09224.

Experimental details, NMR spectra, and other materials, including Scheme S1, Figures S1−S51, and Table S1 (PDF)

AUTHOR INFORMATION

Corresponding Authors

*zwmao@zju.edu.cn
*fhuang@zju.edu.cn
*shawn.chen@nih.gov
*stang@chem.utah.edu

ORCID

Mingming Zhang: 0000-0003-3156-7811
Manik Lal Saha: 0000-0003-2242-3007
Feihe Huang: 0000-0003-3177-6744
Xiaoyuan Chen: 0000-0002-9622-0870
Peter J. Stang: 0000-0002-2307-0576

Notes

The authors declare no competing financial interest.

ACKNOWLEDGMENTS

Dedicated to the memory of George A. Olah. P.J.S. acknowledges the NIH (Grant R01 CA215157) for financial support. Z.M. acknowledges the National Key R&D Program of China (2016YFE0132700) and National Natural Science Foundation of China (51673171) for financial support. X.C. acknowledges the Intramural Research Program of the National Institute of Biomedical Imaging and Bioengineering, and National Institutes of Health (ZIA EB000073) for financial support.

REFERENCES

(1) (a) Inokuma, Y.; Arai, T.; Fujita, M. *Nat. Chem.* **2010**, *2*, 780−783. (b) Zarra, S.; Clegg, J. K.; Nitschke, J. R. *Angew. Chem., Int. Ed.* **2013**, *52*, 4837−4840. (c) Yan, X.; Li, S.; Cook, T. R.; Ji, X.; Yao, Y.; Pollock, J. B.; Shi, Y.; Yu, G.; Li, J.; Huang, F.; Stang, P. J. *J. Am. Chem. Soc.* **2013**, *135*, 14036−14039. (d) Yoshizawa, M.; Klosterman, J. K. *Chem. Soc. Rev.* **2014**, *43*, 1885−1898. (e) Grishagin, I. V.; Pollock, J. B.; Kushal, S.; Cook, T. R.; Stang, P. J.; Olenyuk, B. Z. *Proc. Natl. Acad. Sci. U. S. A.* **2014**, *111*, 18448−18453. (f) Cook, T. R.; Stang, P. J. *Chem. Rev.* **2015**, *115*, 7001−7045. (g) Saha, M.; Yan, X.; Stang, P. J. *Acc. Chem. Res.* **2016**, *49*, 2527−2539.

(2) (a) Eryazici, I.; Moorefield, C. N.; Newkome, G. R. *Chem. Rev.* **2008**, *108*, 1834−1895. (b) Oliveri, C. G.; Ulmann, P. A.; Wiester, M. J.; Mirkin, C. A. *Acc. Chem. Res.* **2008**, *41*, 1618−1629. (c) Therrien, B.; Süss-Fink, G.; Govindaswamy, P.; Renfrew, A. K.; Dyson, P. J. *Angew. Chem., Int. Ed.* **2008**, *47*, 3773−3776. (d) Chakrabarty, R.; Mukherjee, P. S.; Stang, P. J. *Chem. Rev.* **2011**, *111*, 6810−6918. (e) Inokuma, Y.; Kawano, M.; Fujita, M. *Nat. Chem.* **2011**, *3*, 349−358. (f) McConnell, A. J.; Wood, C. S.; Neelakandan, P. P.; Nitschke, J. R. *Chem. Rev.* **2015**, *115*, 7729−7793. (g) Brown, C. J.; Toste, F. D.; Bergman, R. G.; Raymond, K. N. *Chem. Rev.* **2015**, *115*, 3012−3035.

(3) (a) Cook, T. R.; Vajpayee, V.; Lee, M. H.; Stang, P. J.; Chi, K. W. *Acc. Chem. Res.* **2013**, *46*, 2464−2474. (b) Grozav, A.; Balacescu, O.; Balacescu, L.; Cheminel, T.; Berindan- Neagoe, I.; Therrien, B. *J. Med. Chem.* **2015**, *58*, 8475−8490.

(4) (a) Yu, G.; Cook, T. R.; Li, Y.; Yan, X.; Wu, D.; Shao, L.; Shen, J.; Tang, G.; Huang, F.; Chen, X.; Stang, P. J. *Proc. Natl. Acad. Sci. U. S. A.* **2016**, *113*, 13720−13725. (b) Gupta, G.; Das, A.; Park, K. C.; Tron, A.; Kim, H.; Mun, J.; Mandal, N.; Chi, K. W.; Lee, C. Y. *Inorg. Chem.* **2017**, *56*, 4615−4621.

(5) (a) Petros, R. A.; DeSimone, J. M. *Nat. Rev. Drug Discovery* **2010**, *9*, 615−627. (b) Ge, Z.; Liu, S. *Chem. Soc. Rev.* **2013**, *42*, 7289−7325. (c) Torchilin, V. P. *Nat. Rev. Drug Discovery* **2014**, *13*, 813−827. (d) Lim, E.-K.; Kim, T.; Paik, S.; Haam, S.; Huh, Y.-M.; Lee, K. *Chem. Rev.* **2015**, *115*, 327−394. (e) Chen, H.; Zhang, W.; Zhu, G.; Xie, J.; Chen, X. *Nat. Rev. Mater.* **2017**, *2*, 17024.

(6) (a) Kim, J.; Piao, Y.; Hyeon, T. *Chem. Soc. Rev.* **2009**, *38*, 372−390. (b) Kobayashi, H.; Ogawa, M.; Alford, R.; Choyke, P. L.; Urano, Y. *Chem. Rev.* **2010**, *110*, 2620−2640. (c) Robinson, J. T.; Hong, G.; Liang, Y.; Zhang, B.; Yaghi, O. K.; Dai, H. *J. Am. Chem. Soc.* **2012**, *134*, 10664−10669. (d) Rieffel, J.; Chitgupi, U.; Lovell, J. F. *Small* **2015**, *11*, 4445−4461. (e) Aron, A. T.; Loehr, M. O.; Bogena, J.; Chang, C. J. *J. Am. Chem. Soc.* **2016**, *138*, 14338−14346.

(7) (a) Zhelev, Z.; Ohba, H.; Bakalova, R. *J. Am. Chem. Soc.* **2006**, *128*, 6324−6325. (b) Borisov, S. M.; Wolfbeis, O. S. *Chem. Rev.* **2008**, *108*, 423−461. (c) Zhang, X.; Gorl, D.; Stepanenko, V.; Wurthner, F. *Angew. Chem., Int. Ed.* **2014**, *53*, 1270−1274. (d) Liang, J.; Tang, B. Z.; Liu, B. *Chem. Soc. Rev.* **2015**, *44*, 2798−2811.

(8) (a) Hong, Y.; Lam, J. W. Y.; Tang, B. Z. *Chem. Commun.* **2009**, 4332−4353. (b) Hong, Y.; Lam, J. W. Y.; Tang, B. Z. *Chem. Soc. Rev.* **2011**, *40*, 5361−5388. (c) Ding, D.; Li, K.; Liu, B.; Tang, B. Z. *Acc. Chem. Res.* **2013**, *46*, 2441−2453. (d) Hu, R.; Leung, N. L. C.; Tang, B. Z. *Chem. Soc. Rev.* **2014**, *43*, 4494−4562. (e) Mei, J.; Hong, Y.; Lam, J. W. Y.; Qin, A.; Tang, Y.; Tang, B. Z. *Adv. Mater.* **2014**, *26*, 5429−5479.

(9) (a) Yan, X.; Wang, H.; Hauke, C. E.; Cook, T. R.; Wang, M.; Saha, M. L.; Zhou, Z.; Zhang, M.; Li, X.; Huang, F.; Stang, P. J. *J. Am. Chem. Soc.* **2015**, *137*, 15276−15286. (b) Saha, M. L.; Yan, X.; Stang, P. J. *Acc. Chem. Res.* **2016**, *49*, 2527−2539. (c) Yan, X.; Wang, M.; Cook, T. R.; Zhang, M.; Saha, M. L.; Zhou, Z.; Li, X.; Huang, F.; Stang, P. J. *J. Am. Chem. Soc.* **2016**, *138*, 4580−4588. (d) Tian, Y.; Yan, X.; Saha, M. L.; Niu, Z.; Stang, P. J. *J. Am. Chem. Soc.* **2016**, *138*, 12033−12036. (e) Zhou, Z.; Yan, X.; Saha, M. L.; Zhang, M.; Wang, M.; Li, X.; Stang, P. J. *J. Am. Chem. Soc.* **2016**, *138*, 13131−13134. (f) Zhang, M.; Saha, M. L.; Wang, M.; Zhou, Z.; Song, B.; Lu, C.; Yan, X.; Li, X.; Huang, F.; Yin, S.; Stang, P. J. *J. Am. Chem. Soc.* **2017**, *139*, 5067−5074.

(10) (a) Yan, X.; Cook, T. R.; Wang, P.; Huang, F.; Stang, P. J. *Nat. Chem.* **2015**, *7*, 342−348. (b) Mei, J.; Leung, N. L. C.; Kwok, R. T. K.; Lam, J. W. Y.; Tang, B. Z. *Chem. Rev.* **2015**, *115*, 11718−11940. (c) Zhang, M.; Li, S.; Yan, X.; Zhou, Z.; Saha, M. L.; Wang, Y.-C.; Stang, P. J. *Proc. Natl. Acad. Sci. U. S. A.* **2016**, *113*, 11100−11105.

(11) (a) Hu, X.; Hu, J.; Tian, J.; Ge, Z.; Zhang, G.; Luo, K.; Liu, S. *J. Am. Chem. Soc.* **2013**, *135*, 17617−17629. (b) Yu, D.; Zhang, Y.; Mao, Z.; Gao, C. *Macromol. Biosci.* **2013**, *13*, 1413−1421.

(12) (a) Johnstone, T. C.; Lippard, S. J. *J. Am. Chem. Soc.* **2014**, *136*, 2126−2134. (b) Naik, A.; Rubbiani, R.; Gasser, G.; Spingler, B. *Angew. Chem., Int. Ed.* **2014**, *53*, 6938−6941. (c) Johnstone, T. C.; Suntharalingam, K.; Lippard, S. J. *Chem. Rev.* **2016**, *116*, 3436−3486.
(13) Wada, T.; Ohkubo, A.; Mochizuki, A.; Sekine, M. *Tetrahedron Lett.* **2001**, *42*, 1069−1072.
(14) (a) Ferrari, M. *Nat. Rev. Cancer* **2005**, *5*, 161−171. (b) Peer, D.; Karp, J. M.; Hong, S.; Farokhzad, O. C.; Margalit, R.; Langer, R. *Nat. Nanotechnol.* **2007**, *2*, 751−760. (c) Davis, M. E.; Chen, Z.; Shin, D. M. *Nat. Rev. Drug Discovery* **2008**, *7*, 771−782.
(15) Knop, K.; Hoogenboom, R.; Fischer, D.; Schubert, U. S. *Angew. Chem., Int. Ed.* **2010**, *49*, 6288−6308.

DOI: 10.1021/jacs.7b09224
J. Am. Chem. Soc. 2017, 139, 15940−15949